Inferring Structure Factors of Charge Stabilized Colloids from Scattering Using Deep Learning

Chi-Huan Tung,[†] Hsin-Lung Chen,[†] Ming-Ching Chang,[‡] Jan-Michael Carrillo,[¶] Bobby G. Sumpter,[¶] Changwoo Do,[§] and Wei-Ren Chen[*,§]

[†]*Department of Chemical Engineering, National Tsing Hua University, Hsinchu 30013, Taiwan*

[‡]*Department of Computer Science, University at Albany - State University of New York, Albany 12222, New York, USA*

[¶]*Center for Nanophase Materials Sciences, Oak Ridge National Laboratory, Oak Ridge 37831, Tennessee, USA*

[§]*Neutron Scattering Division, Oak Ridge National Laboratory, Oak Ridge 37831, Tennessee, USA*

E-mail: chenw@ornl.gov

Abstract

This paper presents an innovative strategy that utilizes deep autoencoder and classification networks within a deep learning framework to address the potential inversion problem in small angle scattering. To evaluate the performance of our proposed approach, we carry out a detailed case study focusing on charged colloidal suspensions. Our results clearly indicate that our deep learning solution offers a reliable and quantitative method for studying molecular interaction. Moreover, our approach surpasses existing deterministic approaches with respect to both numerical accuracy and computational efficiency. Our work demonstrates the enormous potential of deep learning techniques in tackling complex problems in soft matter structures and beyond.

1

Introduction

The importance of charge association between the supporting electrolyte and macroions in charged colloidal suspensions is widely recognized. The resulting screening of electrostatic interactions plays a critical role in determining the stability of colloidal solutions. According to the classical Derjaguin-Landau-Verwey-Overbeek (DLVO) theory,[1] the primary electrostatic interactions can be divided into two distinct components: the repulsive force arising from the overlap of ionic double layers surrounding the colloidal particles and an attractive force originating from the short-range van der Waals interactions between the constituent molecules of the colloidal particles. This attractive force is commonly referred to as the Hamaker interaction, which exhibits an attractive strength typically on the order of $k_B T$, where k_B is the Boltzmann constant and T is the temperature. The magnitude of the double-layer repulsion at the point of contact is generally several times higher than $k_B T$. In charged colloidal systems with low ionic strength, the spatial arrangement of particles is primarily determined by the repulsive forces generated by the long-range double-layer interactions. By solving the Debye-Hückel equation with the linear approximation,[1] this long-range repulsion is found to take the following expression of a hard sphere model augmented by a Yukawa tail representing the screened Coulomb repulsion:

$$\beta\, V_R(r) = \begin{cases} \infty, & \text{if } r < D \\ A\frac{\exp[-\kappa(r-D)]}{r}, & \text{otherwise} \end{cases} \tag{1}$$

Eqn. (1) incorporates several important parameters: β is the Boltzmann factor defined as the reciprocal of $k_B T$. A is given by the expression $\frac{Z^2 e^2}{\epsilon(1+\frac{\kappa D}{2})^2}$ determined by the charge number Z, the electric charge e, the dielectric constant of the solvent ϵ, the dimensionless inverse Debye screening length κ, and the colloidal diameter D. Eqn. (1) and the associated parameters have been extensively employed to describe the electrostatic behavior in a wide range of charged colloidal systems including ionized nanoparticles, self-assemblies, and biological

systems, providing valuable insights into their properties and interactions.

Given the critical role of the repulsive electrostatic interaction as a starting point for the statistical mechanical description of the thermodynamic properties of charged colloidal systems, experimental determination of $V_R(r)$ becomes of paramount interest. Among the array of available experimental techniques, small angle scattering (SAS) emerges as a prominent approach.[2] The effectiveness of this experimental protocol is predicated on Henderson's theorem, which states that there is a unique one-to-one correspondence between the effective potential and the two-point static correlation functions of the system, such as the inter-particle structure factor $S(Q)$ or its Fourier transform, the radial distribution function, $g(r)$.[3–5]

Within the experimental framework of SAS, $V_R(r)$ is not directly measured. Instead, it is indirectly derived from $S(Q)$. Extensive theoretical efforts have been dedicated to establishing a reliable inversion framework that enables the extraction $V_R(r)$ from the measured $S(Q)$. Since the 1980s, integral equation (IE) theories, specifically the Ornstein-Zernike (OZ) equation,[6] have been continuously developed to addresss the correspondence between $S(Q)$ and $V_R(r)$. However, a fundamental limitation arises from the commonly employed closure approximation, impeding the achievement of high accuracy in potential inversion.[7] This limitation becomes increasingly apparent as systems exhibit higher complexity and collectivity, as often observed in charged colloidal systems. Consequently, it significantly impedes the accurate determination of effective interactions within such systems.

For instance, when attempting to derive $V_R(r)$ from the $S(Q)$ of charged colloidal suspensions, the widely used mean spherical approximation (MSA) closure,[8] along with its enhanced variants like rescaled MSA (RMSA)[9] and penetrating-background corrected RMSA (PB-RMSA),[10] is generally applicable only to weakly charged systems. These methods tend to underestimate the fluid structure in highly concentrated or repulsive colloidal suspensions.[11–14] In particular, when employing the state-of-the-art modified PB-RMSA (MPB-RMSA) closure,[14] we have found that it is challenging to use this closure to obtain $S(Q)$

for systems characterized by κ below 0.1. Furthermore, for colloidal volume fractions exceeding 0.3, there is uncertainty regarding the attainment of a reasonable MSA scaling parameter that satisfies the Gillan condition.[15] Furthermore, the computational efficiency of the MPB-RMSA closure, which is one of the key advantages of the MSA closure, becomes significantly compromised as ϕ increases. Other closure approximations, such as the hypernetted chain (HNC) and Percus-Yevick (PY) closures,[16] consistently deviate from simulation results. HNC underestimates the $S(Q)$, while PY overestimates it.[12] Although the Rogers-Young (RY) closure[17] demonstrates improved quantitative agreement with computational references for moderately charged systems, its efficiency is significantly hindered by the requirement of thermodynamic consistency. Moreover, its applicability is limited by the narrow range of densities where convergence is achieved.[18] Furthermore, in the case of highly collective charged colloidal suspensions, where the Coulombic coupling between colloidal particles and counterions is very strong, IE theories fail to provide a solution.[19] These limitations highlight the inadequacy of existing IE approaches in accurately inverting $V_R(r)$ from the $S(Q)$ of charged colloidal suspensions.

Earlier we propose a data-driven ML framework using Gaussian process regression (GPR)[20,21] to overcome limitations of current deterministic IE analytics. We computationally created an extensive library of structure factors, $\{S(Q)_{training}\}$, treating the associated potential parameters as normally distributed random variables with a covariance matrix $\mathbf{K}$. By quantitatively relating variations in $S(Q)$ to parameter changes through $\mathbf{K}$, we demonstrated that the potential parameters can be probabilistically inferred without relying on specific models.

A regression framework is required for experimentally extracting $V_R(r)$. To this end we have developed an iterative optimization algorithm based on a variational autoencoder (VAE).[22] The VAE uses an encoder-decoder convolutional neural network to generate a diverse set of structure factors, $S_{VAE}(Q)$, that resemble the ground truths $\{S(Q)_{training}\}$. In this context, a set of latent variables is employed for regression analysis. Although the optimized $S_{VAE}(Q)$ achieves quantitative agreement with the measured $S(Q)$ within the probed

Q range, it often exhibits nonphysical features beyond this region, thereby violating the asymptotic behaviors of general $S(Q)$. Consequently, the reliability of inverted parameters may be compromised in such cases.

This report highlights our successful resolution of the challenge through the development of a generative function using a generative model. By incorporating physically significant parameters as inputs, our function generator effectively manages the intricacies involved in potential inversion, surpassing the limitations of conventional IE approaches. The accuracy of our generative model approach has been validated through computational benchmarking, using highly interacting charged colloidal suspensions. Additionally, we present the outcomes of regression analysis based on our generative model approach, employing a series of experimentally measured $I(Q)$ from salt-free solutions comprising highly charged silica particles. This demonstrates the capability of our ML inversion algorithm to capture the complex and highly nonlinear relationship between the potential parameters and experimentally measured scattering cross sections $I(Q)$.

Further details regarding the development of our approach are provided in the next section.

Results

In this section, we will begin by presenting a comprehensive overview of the construction process involved in augmenting a neural network.

Neural network generator of structure factor $S(Q)$

Earlier we developed a variational autoencoder (VAE) to extract expressive features from an extensive set of structure factor $S(Q)$ which were generated computationally in the phase region of equilibrium fluids.[23] The VAE includes an encoder that converts the multi-dimensional input $S(Q)$ to three-dimensional latent variables, and a decoder that recon-
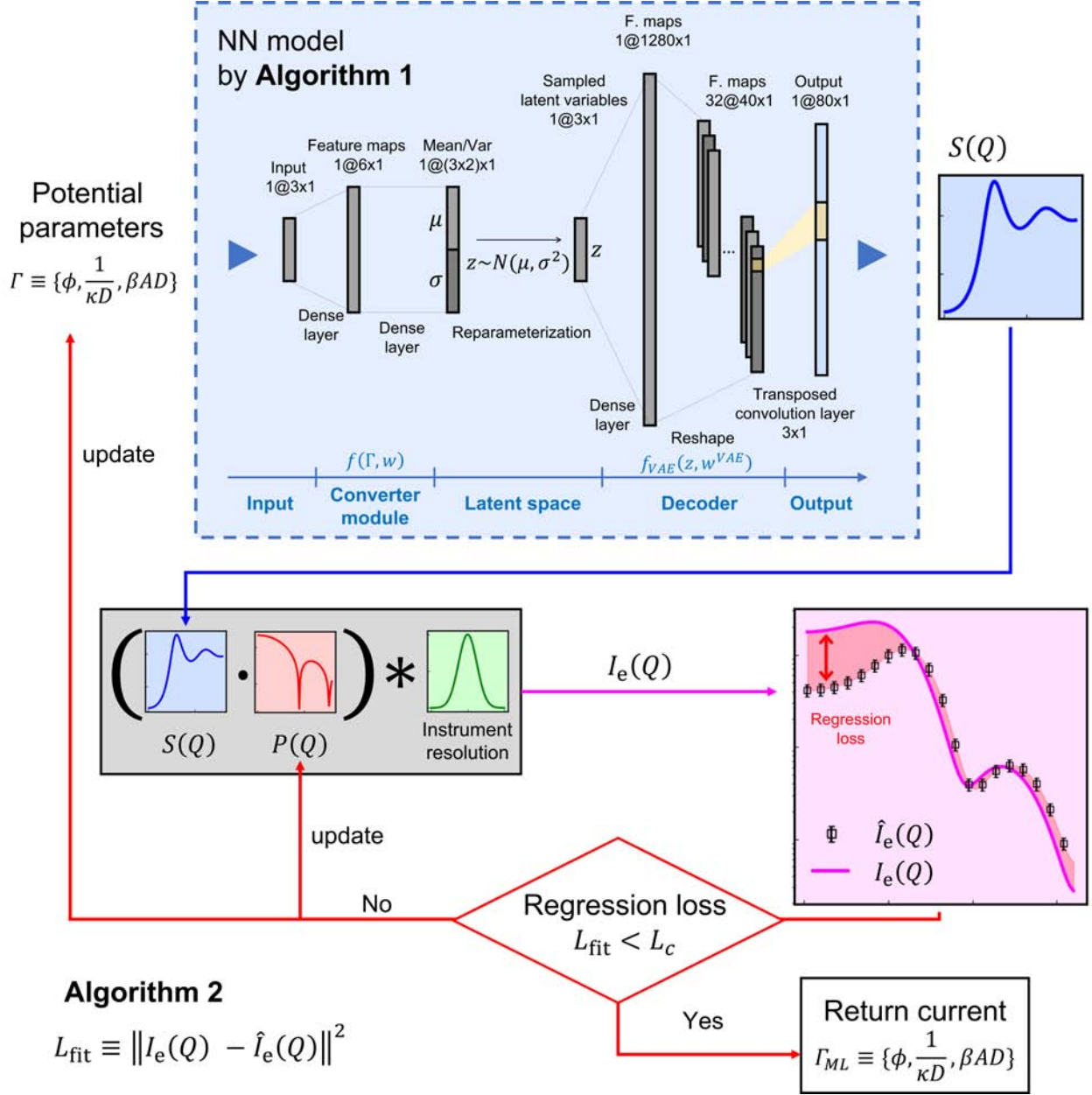
Figure 1: Representation of our neural network (NN) data analysis process for extracting the effective interactions of colloidal suspensions from small angle scattering.

structs the input from the latent variables. Through training, we established a continuous and smooth two-way mapping between $S(Q)$ and latent variables, enabling us to explore the connection between low-dimensional representations of $S(Q)$ and potential parameters that determine the statistical arrangements of colloidal particles.

To build upon our pre-trained VAE model, we utilized transfer learning and developed

Algorithm 1: Training the $S(Q)$ generator

Input: $\hat{\Gamma}$, $\hat{S}(Q)$, VAE decoder f_{VAE} with weights w_0^{VAE}, converter module f with weights w_0

Result: Optimal w and w^{VAE} such that
$$S_{\text{ML}}(Q) = f_{\text{NN}}(Q, \Gamma) \equiv f_{\text{VAE}}(Q, w^{\text{VAE}}, f(\Gamma, w))$$

1   $w^{\text{VAE}} \leftarrow w_0^{\text{VAE}}$;   `// initialize VAE decoder`

2   $w \leftarrow w_0$;   `// initialize Converter module`

3   $i \leftarrow 0$

4   **while** $i <$ Maxiter **do**

5      $z \leftarrow f(\hat{\Gamma}, w)$;   `// convert` $\hat{\Gamma}$ `to latent variable`

6      $S_{\text{ML}}(Q) \leftarrow f_{\text{VAE}}(z, w^{\text{VAE}})$;   `// generate S(Q)`

7      $L \leftarrow \left\| S_{\text{ML}}(Q) - \hat{S}(Q) \right\|^2$;   `// evaluate loss function`

8   Freeze w^{VAE}, update w with `Adam` optimizer to minimize L

9      $i \leftarrow i + 1$

10   **end**

11   Unfreeze w^{VAE}

12   $i \leftarrow 0$

13   **while** $i <$ Maxiter **do**

14      $z \leftarrow f(\hat{\Gamma}, w)$;   `// convert` $\hat{\Gamma}$ `to latent variable`

15      $S_{\text{ML}}(Q) \leftarrow f_{\text{VAE}}(z, w^{\text{VAE}})$;   `// generate S(Q)`

16      $L \leftarrow \left\| S_{\text{ML}}(Q) - \hat{S}(Q) \right\|^2$;   `// evaluate loss function`

17      $L' \leftarrow L + \alpha \left\| w^{\text{VAE}} \right\|^2$;   `// regularization`

18   Update w, w^{VAE} with `Adam` optimizer to minimize L'

19      $i \leftarrow i + 1$

20   **end**

---

an generative neural network (NN) architecture highlighted by the blue background in Fig. 1 that connects the pre-trained decoder f_{VAE} with a converter module f composed of a shallow fully connected NN. The weights associated with f_{VAE} and f are represented by w_{VAE} and w, respectively. Throughout this report, the symbol ˆ is used to denote any quantities or functions associated with the computationally generated ground truth. Initially, the input potential parameters, denoted as $\hat{\Gamma}$, are transformed into latent variables, denoted as z, through the function $f(\hat{\Gamma}, w)$. These latent variables then serve as input to the function f_{VAE}, which generates the output $S_{\text{ML}}(Q) = f_{\text{VAE}}(z, w^{\text{VAE}})$. The training steps of this generator is described in Algorithm 1. In the first step, w^{VAE} is fixed, and w is updated using a gradient descent

`Adam` optimizer[24] to minimize the squared difference $L = \left\| S_{\text{ML}}(Q) - \hat{S}(Q) \right\|^2$ between the output of the augmented NN model $S_{\text{ML}}(Q)$ and $\hat{S}(Q)$. This step is repeated until the maximum number of iterations, is reached. Next, both w and w^{VAE} are updated simultaneously using the `Adam` optimizer. The optimization objective $L' = \left\| S_{\text{ML}}(Q) - \hat{S}(Q) \right\|^2 + \alpha \left\| w^{\text{VAE}} \right\|^2$ includes the squared difference between the output $S_{\text{ML}}(Q)$ and $\hat{S}(Q)$ as well as a regularization term, $\left\| w^{\text{VAE}} \right\|^2$ with $\alpha = 0.05$, which encourages small values for w^{VAE}. Again, this step continues until the maximum number of iterations is reached. By iterating through these steps, the algorithm aims to converge towards the optimal values for w and w^{VAE}, achieving the desired similarity between $S_{\text{ML}}(Q)$ and $\hat{S}(Q)$ as well as controlling the magnitude of w^{VAE}. This augmented NN model captures the non-linear relations between potential parameters and latent variables, while retaining the variational feature to account for random noises inherent in the molecular dynamics-generated training sets. After the training and fine-tuning as shown in Algorithm 1, the resulting NN model can generate $S(Q)$ curves that correspond to input potential parameters.

Computational Evaluation of Numerical Accuracy

After introducing the architecture of the NN $S(Q)$ model, our focus now shifts to evaluating its performance as a part of potential inversion algorithm. To accomplish this, we employ the mean squared error (MSE) as a metric to assess the accuracy of the ML-generated structure factor, denoted as $S_{ML}(Q)$ for charged colloidal suspensions. This benchmarking involves a comprehensive comparison between $S_{ML}(Q)$ and the corresponding ground truth $\hat{S}(Q)$ obtained through MD simulations generated based on the identical potential parameters.

$$MSE = \frac{1}{n} \sum_{i=1}^{n} (e_i)^2 = \frac{L}{n} \tag{2}$$

where e_i representing the numerical difference between the ith sampled Q point of $S_{ML}(Q)$ and that of $\hat{S}(Q)$. For each $S_{ML}(Q)$ and $\hat{S}(Q)$, 80 Q points are sampled within the range
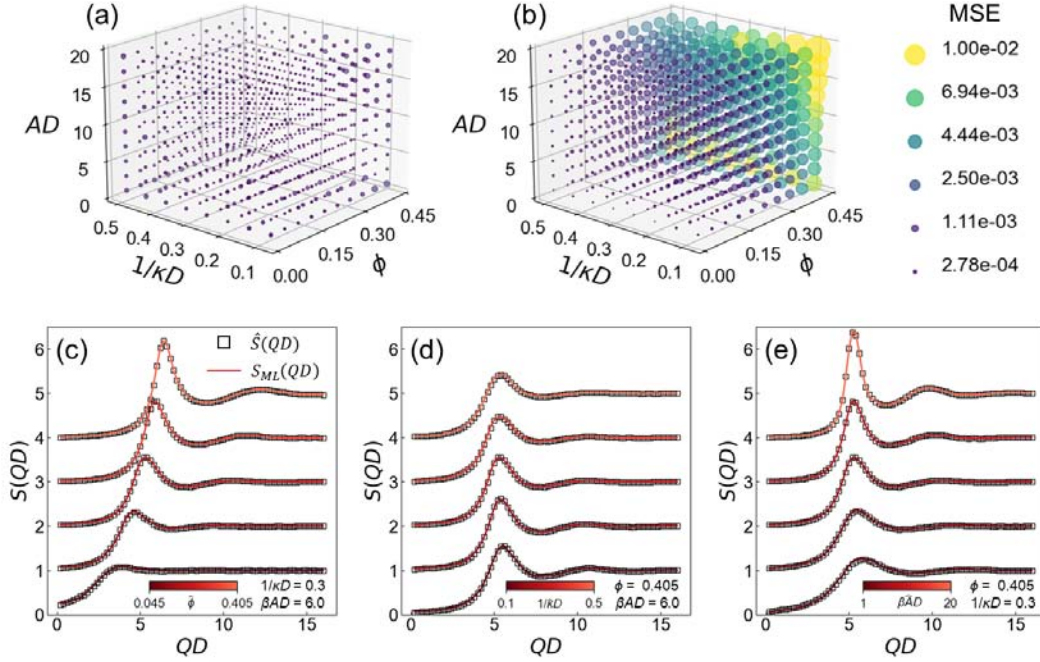
Figure 2: Panels (a) and (b) display the mean squared error (MSE) between the ground truth $\hat{S}(Q)$ generated computationally and that produced by the machine learning and OZ-RMSA methods, respectively. Within the probed equilibrium fluid region, the quantitative accuracy of the $S(QD)$ generated by OZ-RMSA is seen to deteriorate rapidly upon increasing ϕ and A. Panels (c), (d) and (e) display the ground truths $\hat{S}(QD)$ (black curves) and ML-generated $S(QD)$ (red curves) for the selected phase regions with the corresponding system parameters being indicated in the legends.

of interest, therefore $n = 80$. The calculated results are presented in a dimensionless scaled format of QD where D is the colloidal diameter. The domains of relevant parameter $\{\phi, \frac{1}{\kappa D}, \beta AD\} \equiv \hat{\Gamma}$ are chosen according to[23] to ensure the simulated system remains in the equilibrium fluid phase. According to Eqn. (2), MSE therefore measures the deviation from the square of Euclidean distance in the vector space of structure factor with demension of 80. As indicated by Panel (a) of Fig. 2, the MSE is seen to be no greater than $\sim 4 \times 10^{-4}$. The root-mean-square error (RMSE), which has the same unit as the evaluated $S_{ML}(Q)$, can be obtained by taking the square root of the MSE. Consequently, we conclude that the overall numerical error of the $S_{ML}(Q)$ in the probed phase region is less than 2%. It is crucial to note that the degree of uncertainty is determined collectively by the inherent noise

present in the simulated $\hat{S}(QD)$ and the precision of the ML inversion algorithm outlined in Algorithm 1.

To demonstrate the superior accuracy and precision of the ML inversion algorithm in comparison to conventional IE approaches, the OZ-RMSA approach[9] was used to generate the structure factor termed as $S_{RMSA}(QD)$. In this context, precision denotes the measure of inverted mean, while accuracy represents the measure of variance pertaining to the inverted parameters, relative $\hat{\Gamma}$. This comparison serves to establish the robustness and reliability of the ML approach. The reason for selecting OZ-RMSA approach in this benchmarking purpose is due to its wide acceptance for inverting the effective interaction of charged colloidal suspensions from small angle scattering, as evidenced by its integration into the SasView user interface. The evaluation results against the corresponding ground truth $\hat{S}(QD)$ are presented in Panel (b) of Fig. 2, which clearly demonstrate that the OZ-RMSA approach is only applicable to weakly interacting systems when used as a potential inversion framework. Our observations indicate that as the level of structural collectivity increases, either by augmenting ϕ or A, the extent of discrepancy escalates significantly. Panels (c), (d), and (e) depict the ground truth $\hat{S}(QD)$ (the black curves) and $S_{ML}(QD)$ (the red curves) for the selected phase regions. The legends provide the respective system parameters. Quantitative agreement is observed within the probed QD range.

Application for Practical Potential Inversion Problem

In order to further verify the feasibility of the ML approach in potential inversion problem of practical experiment, the small angle neutron scattering cross sections $\hat{I}(Q)$ are calculated from the corresponding $\hat{S}(Q)$ via the following expression:

$$\hat{I}(Q) = n_c \Delta \rho^2 v^2 P(Q) \hat{S}(Q) + I_{inc} \tag{3}$$

where n_c is the number density of colloidal particles, $\Delta\rho$ the difference between the scattering length density of a colloidal particle and that of solvent, v the volume of a colloidal particle, $P(Q)$ the normalized form factor which describe the intra-particle spatial correlation. In this study we model the colloidal particle as a homogeneous hard sphere, therefore the form factor $P(Q)$ is given by

$$P(Q) = [3\frac{j_1(QR)}{QR}]^2 \tag{4}$$

where $R = \frac{D}{2}$ and $j_1(x)$ is the Bessel function of the first kind with an order of 1 for argument x. I_{inc} is the incoherent background. It is instructive to note that Eqn. (3) is only valid when the system is composed of monodisperse spherical objects. To account for the effect of instrumental smearing, $\hat{I}(Q)$ given in Eqn. (3) is further convoluted with the resolution function:

$$\hat{I}_e(Q) = \int_0^\infty \frac{\hat{I}(Q)}{\sqrt{2\pi\sigma_R^2(Q)}} \exp[-\frac{(Q-Z)^2}{2\sigma_R^2(Q)}]dZ \tag{5}$$

The quantity $\sigma_R(Q)$ represents the width of the resolution function that accounts for the smearing of spatial resolution. The subscript e signifies the use of Eqn. (5) to represent the experimental small angle neutron scattering cross sections in this report. It is important to note that due to the ill-posed nature of deconvolution, it is not practical to extract $\hat{I}(Q)$ from $\hat{I}_e(Q)$ in a mathematically unique manner. Therefore, to minimize numerical errors, one commonly adopted implementation for potential inversion involves performing data-driven regression analysis directly on $\hat{I}_e(Q)$.

Implementation of Curve Fitting

Our ML method provides a numerical estimation of structure factor without relying on any *a priori* assumptions of mathematical expression, making it a valuable replacement for the popular IE approaches. The model's ability to incorporate into the standard least-square curve fitting procedure for potential inversion given by Algorithm 2 in Fig. 1 is also noteworthy. The curve fitting algorithm initializes Γ, $P(Q)$, and I_{inc} with the initial guesses

11

Algorithm 2: Potential inversion by least squares curve fitting

Input: $\hat{I}_e(Q)$, $f_{\mathrm{NN}}(Q)$, initial guesses $x^{\mathrm{i}} = \{\Gamma^{\mathrm{i}}, P^{\mathrm{i}}(Q), I_{\mathrm{inc}}^{\mathrm{i}} C^{\mathrm{i}}\}$, instrument resolution $\sigma_R(Q)$

Result: Γ_{ML}

1 $\Gamma \leftarrow \Gamma^{\mathrm{i}}$
2 $P(Q) \leftarrow P^{\mathrm{i}}(Q)$
3 $I_{\mathrm{inc}} \leftarrow I_{\mathrm{inc}}^{\mathrm{i}}$;   // initial guess
4 $C \leftarrow C^{\mathrm{i}}$
5 $i \leftarrow 0$
6 **while** $i <$ Maxiter **do**
7 $S_{\mathrm{ML}}(Q) \leftarrow f_{\mathrm{NN}}(Q, \Gamma)$;   // generate S(Q)
8 $I(Q) \leftarrow C P(Q) S(Q) + I_{\mathrm{inc}}$ (Eqn. 3) ;   // generate I(Q)
9 $I_e(Q) \leftarrow \int_0^\infty \frac{I(Q)}{\sqrt{2\pi\sigma_R^2(Q)}} \exp[-\frac{(Q-Z)^2}{2\sigma_R^2(Q)}] dZ$ (Eqn. 5) ;   // apply resolution
10 $L_{\mathrm{fit}} \leftarrow \left\| I_e(Q) - \hat{I}_e(Q) \right\|^2$;   // evaluate regression loss
11   Update Γ, $P(Q)$, I_{inc} and C with `L-BFGS-B` algorithm to minimize L_{fit}
12 $i \leftarrow i + 1$
13   **if** $L_{\mathrm{fit}} < L_c$ **then**
14 $\Gamma_{\mathrm{ML}} \leftarrow \Gamma$;   // return the fitting result
15   **end**
16 **end**

provided. It then enters a loop where it iteratively updates these parameters. Within each iteration, the algorithm calculates $S_{\mathrm{ML}}(Q)$ based on the current values of Γ using the neural network framework. It then computes the estimated scattering cross section $I_e(QD)$ according to Eqn. 5. The algorithm measures the discrepancy between the $I_e(QD)$ and $\hat{I}_e(QD)$ using the squared difference L defined in step 10 of Algorithm 2. It updates the parameters Γ, $P(Q)$, I_{inc}, and C using the limited-memory Broyden–Fletcher–Goldfarb–Shanno bound-constrained (L-BFGS-B) optimization algorithm [25] implemented in SciPy [26] to minimize L_{fit}. If the discrepancy L_{fit} falls below a certain threshold L_c, the algorithm sets the current value of Γ as the estimate Γ_{ML}.
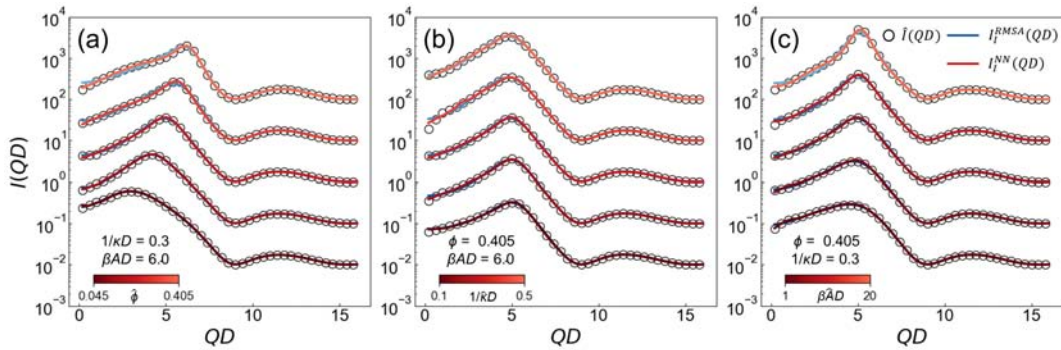

Figure 3: Panels (a), (b) and (c) give the small angle coherent scattering cross sections of charged colloidal suspensions in selected phase regions. The squares represent the ground truths $\hat{I}_e(QD)$ generated by MD simulation. Additionally, the red solid curves and blue dashed curves represent the best-fitted curves obtained from regression analyses based on the ML approach and OZ-RMSA integral equation, respectively. All $I(QD)$ have been vertically adjusted for the purpose of facilitating visual examination.

In Fig. 3, we provide illustrative examples of such analyses carried out using two different methods - the ML inversion algorithm and the OZ-RMSA integral equation, over the target of $\hat{I}_e(QD)$. Panels (a), (b), and (c) display a comparison between the ground truths $\hat{I}_e(QD)$ (the open squares), the best-fitted curves obtained from the ML approach (the red curves), and the OZ-RMSA integral equation (the blue curves), respectively. Both the ML and OZ-RMSA approaches are seen to offer quantitatively accurate representations of $\hat{I}_e(QD)$. In 16 and 16, we present the values of $\{\phi, \kappa, A\}$ extracted from the ML approach and the OZ-RMSA method respectively. Overall, the ML inversion algorithm in regression analysis of

$\hat{I}_e(QD)$ accurately extracts all $\{\phi, \kappa, A\}$ except for some certain cases where a deviation of $\sim 20\%$ in κ and A is observed, as indicated in 16. In contrast, while the OZ-RMSA approach is able to precisely determine ϕ, its inherent deficiency as an inversion algorithm is evident in the noticeable deviation in extracted κ and severe disagreement in extracted A, as revealed by the results given in 16.

Insights into the Numerical Precision and Accuracy of Inverted Potential

While the pronounced discrepancy observed between $\hat{\Gamma}$ and Γ^I_{RMSA} given in 16 (Here the superscript I and subscript $RMSA$ in Γ^I_{RMSA} indicate that these parameters were obtained through regression analyses of $\hat{I}_e(QD)$ using the OZ-RMSA approach) has been recognized to originate from the approximate of the closure relation employed in the OZ equation, the factors contributing to the inconsistency between $\hat{\Gamma}$ and Γ^I_{ML} displayed in 16, although relatively small in magnitude, still lack clarity. Therefore, conducting a comprehensive investigation to uncover the underlying cause of this inconsistency is crucial. To this end, we conducted a comprehensive analysis of the phase point specified by $\{\phi, \kappa, A\}$ as detailed in row xii of Γ^I_{ML} in 16. Using this set of inverted parameters, we generated a plot illustrating the effective interaction $V_I(r/D)$. Here the subscript I indicates the associated parameters were obtained from the regression analysis of $\hat{I}_e(QD)$. By directly comparing this plot with $\hat{V}(r/D)$, we can assess their agreement. The results presented in Panel (a) of Fig. 4 indeed demonstrate a noticeable discrepancy between $\hat{V}(r/D)$ (the black dashed curve) and $V_I(r/D)$ (the red curve). This disparity exceeds the anticipated range of experimental uncertainties, clearly indicating a significant deviation between the two.

Panel (b) presents a comprehensive comparison between the structure factor, obtained from the regression analysis of $\hat{I}_e(QD)$, denoted as $S_I(QD) \equiv S_{\mathrm{ML}}(QD, \Gamma^I_{\mathrm{ML}})$, and its corresponding ground truth $\hat{S}(QD)$ represented by the black squares. While a quantitative agreement is clearly observed between $\hat{I}_e(QD)$ and optimized curve $I_I(QD)$ (the orange curve) as indicated by the inset, a subtle discrepancy is observed around the first correlation
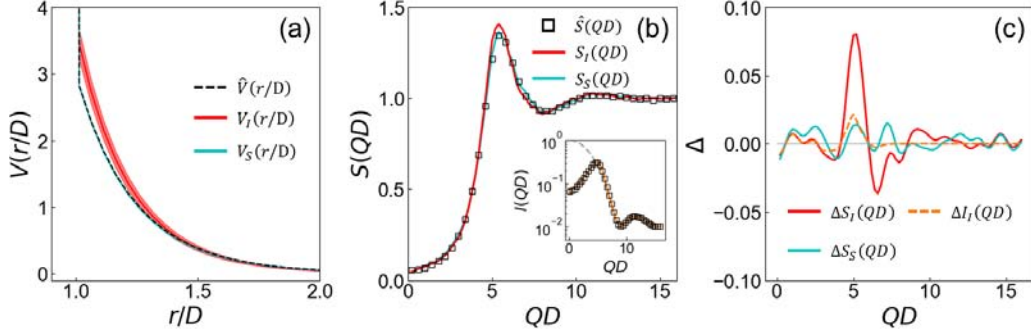
Figure 4: (a): A comparison between $\hat{V}(r/D)$ (the black dashed curve), $V_I(r/D)$ inverted from the regression analysis of $\hat{I}_e(QD)$ (the red curve), and $V_S(r/D)$ inverted from the regression analysis of $\hat{S}(QD)$ (the cyan curve). (b): A comparison between the $\hat{S}(QD)$ (the black squares), $S_I(QD)$, the structure factor obtained from the regression analysis of $\hat{I}(QD)$ (the red curve), and $S_S(QD)$, the structure factor optimized from the regression analysis of $\hat{S}(QD)$ (the cyan curve). A comparison between the $\hat{I}_e(QD)$ (the black squares) and the optimized $I_I(QD)$ (the red curve), along with the associated $P(Q)$ (the gray dashed curve) are given in the inset. (c) The residual plots presenting the vertical deviations between $\hat{S}(QD)$ and $S_I(QD)$ (the red solid curve), $\hat{S}(QD)$ and $S_S(QD)$ (the cyan curve), and $\hat{I}(QD)$ and $I_I(QD)$ (the orange dashed curve).

peak, occurring at approximately $QD \sim 6$. This observation evidences the substantial influence of $P(Q)$ (the gray dashed curve in the inset) on the outcomes of the regression analysis for potential inversion of $\hat{I}_e(QD)$ which represents the experimentally measured scattering cross section. When employing $\hat{I}_e(QD)$ as the target function, the accuracy of the inverted Γ^I_{ML} presented in 16 is inevitably impacted by the loss of expressive features exhibited by $\hat{S}(QD)$ in the high Q region of $QD \gtrsim 6$. According to Eqn.(4), for this illustrative example the coherent intensity of $P(Q)$ decreases as Q^{-2} as a function of Q within this QD region, while $S(QD)$ oscillates characteristically around the asymptotic value of $S(QD \to \infty) = 1$. Consequently, based on Eqn.(3), certain distinct features of $S(QD)$ are unavoidably smeared due to the rapid decay of $P(Q)$ and the presence of I_{inc}.

To provide further support for this argument, we selected $\hat{S}(QD)$ as the target function and conducted complementary regression analysis accordingly. The corresponding results referred as Γ^S_{ML} are provided in 16. Here, the superscript S is used to indicate that the target function is $\hat{S}(QD)$ rather than $\hat{I}_e(QD)$. From the result given in Panel (b) of Fig. 4,

the optimized curve $S_S(QD) \equiv S_{\mathrm{ML}}(QD, \Gamma_{\mathrm{ML}}^S)$ is found to exhibit a discernible quantitative agreement with $\hat{S}(QD)$, as depicted by the cyan curve. The previously observed approximately 20% discrepancy in A reported in 16 is essentially eliminated in the results reported in 16. Moreover, as illustrated in Panel (a), the reconstructed effective potential $V_S(r/D)$ (the cyan curve) exhibits a quantitative agreement with the ground truth $\hat{V}(r/D)$ (the black dashed curve). Panel (c) of Fig. 4 further presents the residual plot to measure the vertical disagreement between the ML-inferred spatial correlation functions and the corresponding ground truths within the Q range of interest. Namely,

$$
\begin{aligned}
\Delta S(Q) &= S(Q) - \hat{S}(Q) \\
\Delta I(Q) &= I_e(Q) - \hat{I}_e(Q)
\end{aligned}
\tag{6}
$$

By analyzing the data presented in Panel (b) of Fig. 4, $\Delta I_I(QD)$ can be calculated according to Eqn.(6); Two important features of $\Delta I_I(QD)$ are revealed by the results represented by the red dashed curve in Panel (c): First, $\Delta I_I(QD)$ is essentially zero when $QD \gtrsim 6$, suggesting that $\hat{I}_e(QD)$ is virtually identical to $I_I(QD)$ in this high Q region. It thus evidences the coherent signal is predominantly governed by $P(Q)$ in both correlation functions. The QD region containing statistically meaningful data of $S(QD)$ for potential inversion is thus limited to the range of $QD \lesssim 6$. The magnitude of $\Delta S_I(QD)$ generated from the regression analysis of $\hat{I}_e(QD)$ is considerably greater than that of $\Delta S_S(QD)$ obtained from the regression analysis of $\hat{S}(QD)$. As a result, the deviations in Γ_{ML}^I are more pronounced compared with those in Γ_{ML}^S. Secondly, within the statistically relevant range, both $\Delta I_I(QD)$ and $\Delta S_S(QD)$ are found to be consistently no greater than 0.02. This magnitude is essentially identical to the RMSE deduced from the MSE provided in Panel (a) of Fig. 2. Hence, it is evident that there is no room for further improvement in the quantitative agreement in $\Delta I_I(QD)$ or $\Delta S_S(QD)$, the regression analysis based on the NN generated $S(Q)$ has reached its inherent precision limit. This implies that the numerical difference between $\hat{\Gamma}$ and the inverted Γ_{ML}^I given in 16 can not be further minimized.

It is important to note that there has been much interest in developing model-free techniques for potential inversion. These techniques, such as iterative Boltzmann inversion, force matching, relative entropy minimization, as well as the other machine learning approaches, aim to overcome the inherent limitations of the existing OZ integral equation approaches. Our findings, as illustrated in Fig. 4, hold significant implications for these non-parametric theoretical endeavors as well: Within the framework of this data analysis protocol, an additional regression analysis on the inverse function $V_R(r)$ based on the parametric screened Coulomb formula is necessary. This analysis allows for the extraction of important information regarding the effective charge, which holds relevance for experimentalists. To ensure the practical application of these model-free approaches for potential inversion using small-angle scattering, it is crucial to consider the combined impact of factors such as $P(Q)$, instrument resolution, as well as statistical noise from the detector. This consideration enables a numerically reliable evaluation of the effective charge while accurately assessing the mean and variance of the inverted function $V_R(r)$. By incorporating these considerations, the model-free approaches can be improved in terms of their practicality and reliability for accurately inverting the potential of charged colloidal suspensions from their small-angle scattering cross sections.
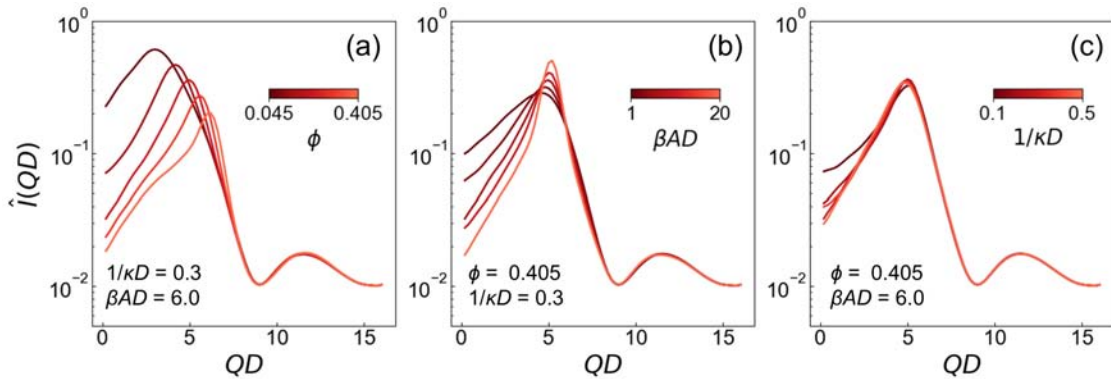

Figure 5: The evolution of $I(QD)$ as a function of (a) ϕ, (b) βAD, and (c) $\frac{1}{\kappa D}$. The ranges of parameters are given by the legends.

Moreover, the comparison between Γ_{ML}^I in 16 and Γ_{ML}^S in 16 reveals that changing the target function from $\hat{I}_e(QD)$ to $\hat{S}(QD)$ did not improve the agreement between the inverted

κ and the corresponding ground truths. To understand the underlying reasons for this observation, we conduct an analysis to assess the sensitivity of $\hat{I}(QD)$ to variations in ϕ, κ, and A. The findings are presented in Fig. 5. Within the explored parameter ranges, adjusting ϕ causes a noticeable shift in the primary correlation peak of $\hat{I}(QD)$, as illustrated in Panel (a). Furthermore, Panel (b) demonstrates that an increase in A leads to a clear narrowing of its width. However, Panel (c) indicates that the effect of varying κ on the evolution of $\hat{I}(QD)$ is less pronounced. Apart from the extreme case of $\frac{1}{\kappa D} = 0.1$, where substantial changes in the intensity of $\hat{I}(QD)$ occur when $QD < 0.3$, the variation of κ only induces minor alterations in the intensity of $\hat{I}(QD)$ in the low Q region. This observation suggests that the potential difference caused by the change in κ does not render sufficient structural change in terms of two-point static correlation. Fig. 5 reveals the difference in the responsiveness of the two-point static correlation function toward the variation in different parameters. To us investigating the posedness of different variables in potential inversion problem is of interest in its own right. We intend to delve into this topic in future research endeavors.

Concluding Discussion

In conclusion, we have developed a novel deep learning inversion framework that leverages the mathematical principles of neural networks (NN) to accurately determine the effective interaction of charged colloidal suspensions from their scattering cross sections. Our approach surpasses the limitations of existing integral equation (IE) methods, which struggle to effectively address the structure-interaction correspondence in charged colloidal suspensions. By using an extensive library of structure factors generated computationally as the training set, our framework overcomes the shortcomings of traditional IE approaches. Unlike the laborious numerical calculations involved in current IE methods, our approach based on a deep autoencoder and a classification network employs a series of matrix operations to invert

potential parameters from the experimentally measured scattering cross sections. This not only enhances numerical accuracy but also significantly improves computational efficiency, making our approach a more practical and widely applicable solution of potential inversion.

This research also highlights a promising avenue for future investigation: The DLVO potential, which encompasses a long-range Coulombic repulsion, as described in Eqn. (1), and a short-range van der Waals attraction, has been proven to be an effective theoretical framework for understanding the properties of charged colloidal suspensions. The nature of charged colloidal suspensions depends on the ionic strength. At low ionic strength, the repulsive component dominates and underpins the stability of highly charged systems. An increase in the ionic strength results in the dominance of the attractive part of the potential at short distances, thus leading to phenomena such as flocculation and dynamical clustering. Our current method offers a comprehensive solution to the potential inversion problem for charged colloidal suspensions under low ionic conditions. In combination with computer simulations of both double-layer repulsion and dispersive attraction, which account for the general radial dependence of electrostatic interactions, our ML approach can be systematically expanded to address potential inversion challenges in diverse charged colloidal systems, encompassing a wide range of ionic conditions commonly encountered in experimental scenarios. By advancing the field of colloidal structural study and offering new possibilities for research and applications of molecular interaction using scattering techniques, our approach contributes significantly to the ongoing progress in this domain.

Moreover, the current investigation not only establishes a sturdy framework for examining the effective interaction among charged colloidal suspensions but also uncovers a highly promising pathway for future exploration. Previous experimental and computational studies[27,28] have demonstrated the presence of many-body interactions within charged colloidal suspensions, underscoring their vital implications that demand comprehensive consideration when elucidating the intricate phase behaviors of such systems. It remains unexplored whether the measured two-point correlation functions, which collectively manifest the pair-

wise and many-body interactions at the particle level, can provide information regarding multi-particle interactions. Providing the mathematical expression of many-body interaction, our ML potential inversion framework presents a promising approach for directly mapping this information using elastic scattering experiments complemented by computer simulations.

Acknowledgement

Supporting Information Available

Comparison of the Potential Parameters Inverted from the Regression Analysis of $\hat{I}(QD)$ by ML Approach and the Ground Truths $\hat{\Gamma}$

| | $\hat{\Gamma}$ | | | | Γ_{ML}^{I} | | | |
	$\hat{\phi}$	$1/\hat{\kappa}D$	$\beta\hat{A}D$	$\hat{Z}$	$\phi/\hat{\phi}$	$\hat{\kappa}/\kappa$	$A/\hat{A}$	$Z/\hat{Z}$
i	0.045	0.300	6.000	6.532	1.005±0.021	1.046±0.052	1.000±0.002	0.972±0.030
ii	0.135	0.300	6.000	6.532	1.023±0.014	1.288±0.095	0.950±0.024	0.839±0.036
iii	0.225	0.300	6.000	6.532	0.999±0.014	1.067±0.061	1.090±0.047	1.003±0.041
iv	0.315	0.300	6.000	6.532	0.997±0.011	1.072±0.072	1.150±0.024	1.028±0.043
v	0.405	0.300	6.000	6.532	1.004±0.008	1.115±0.065	1.092±0.034	0.977±0.037
vi	0.225	0.100	6.000	14.697	0.999±0.011	1.253±0.060	1.000±0.002	0.832±0.032
vii	0.225	0.200	6.000	8.573	1.029±0.008	1.561±0.074	1.001±0.002	0.744±0.022
viii	0.225	0.300	6.000	6.532	0.999±0.014	1.067±0.061	1.090±0.047	1.003±0.041
ix	0.225	0.400	6.000	5.511	1.047±0.051	1.250±0.025	1.068±0.069	0.919±0.031
x	0.225	0.500	6.000	4.899	0.991±0.007	0.800±0.019	1.000±0.002	1.125±0.015
xi	0.225	0.300	1.000	2.667	0.964±0.015	0.913±0.039	1.000±0.010	1.060±0.030
xii	0.225	0.300	3.000	4.619	0.971±0.015	0.891±0.038	1.226±0.076	1.192±0.050
xiii	0.225	0.300	6.000	6.532	0.999±0.014	1.067±0.061	1.090±0.047	1.003±0.041
xiv	0.225	0.300	10.000	8.433	1.010±0.010	1.132±0.047	0.985±0.032	0.920±0.027
xv	0.225	0.300	20.000	11.926	1.006±0.008	1.133±0.029	1.000±0.001	0.926±0.014

Comparison of the Potential Parameters Inverted from the Regression Analysis of $\hat{I}(QD)$ by OZ-RMSA and $\hat{\Gamma}$

| | $\hat{\Gamma}$ | | | | $\Gamma_{OZ-RMSA}$ | | | |
	$\hat{\phi}$	$1/\hat{\kappa}D$	$\beta\hat{A}D$	$\hat{Z}$	$\phi/\hat{\phi}$	$\hat{\kappa}/\kappa$	$A/\hat{A}$	$Z/\hat{Z}$
i	0.045	0.300	6.000	6.532	0.994±0.107	1.598±0.224	0.549±0.147	0.568±0.086
ii	0.135	0.300	6.000	6.532	0.976±0.026	1.260±0.092	0.934±0.080	0.842±0.050
iii	0.225	0.300	6.000	6.532	0.988±0.018	1.088±0.069	0.960±0.048	0.930±0.043
iv	0.315	0.300	6.000	6.532	1.004±0.010	1.520±0.147	0.767±0.038	0.689±0.039
v	0.405	0.300	6.000	6.532	0.956±0.005	1.667±0.033	0.639±0.034	0.600±0.017
vi	0.225	0.100	6.000	14.697	0.990±0.045	1.760±0.324	0.673±0.111	0.525±0.083
vii	0.225	0.200	6.000	8.573	0.997±0.018	1.448±0.102	0.936±0.050	0.754±0.039
viii	0.225	0.300	6.000	6.532	0.988±0.018	1.088±0.069	0.960±0.048	0.930±0.043
ix	0.225	0.400	6.000	5.511	0.988±0.015	1.250±0.025	1.063±0.039	0.916±0.019
x	0.225	0.500	6.000	4.899	0.983±0.017	0.892±0.049	0.896±0.045	1.004±0.039
xi	0.225	0.300	1.000	2.667	0.953±0.014	1.667±0.033	1.225±0.082	0.830±0.029
xii	0.225	0.300	3.000	4.619	0.974±0.022	1.093±0.106	1.016±0.091	0.954±0.070
xiii	0.225	0.300	6.000	6.532	0.988±0.018	1.088±0.069	0.960±0.048	0.930±0.043
xiv	0.225	0.300	10.000	8.433	0.996±0.015	1.128±0.073	0.902±0.045	0.882±0.040
xv	0.225	0.300	20.000	11.926	1.002±0.013	0.947±0.087	0.818±0.046	0.936±0.061

Comparison of the Potential Parameters Inverted from the Regression Analysis of $\hat{S}(QD)$ by ML Approach and $\hat{\Gamma}$

			$\hat{\Gamma}$		Γ_{ML}^S			
	$\hat{\phi}$	$1/\hat{\kappa}D$	$\beta\hat{A}D$	$\hat{Z}$	$\phi/\hat{\phi}$	$\hat{\kappa}/\kappa$	$A/\hat{A}$	$Z/\hat{Z}$
i	0.045	0.300	6.000	6.532	1.019±0.048	1.005±0.030	1.000±0.002	0.997±0.018
ii	0.135	0.300	6.000	6.532	0.983±0.046	0.950±0.043	1.000±0.002	1.033±0.030
iii	0.225	0.300	6.000	6.532	1.002±0.018	0.989±0.086	1.000±0.002	1.007±0.055
iv	0.315	0.300	6.000	6.532	0.996±0.008	0.947±0.016	1.000±0.001	1.035±0.011
v	0.405	0.300	6.000	6.532	0.996±0.005	0.990±0.022	1.000±0.002	1.006±0.014
vi	0.225	0.100	6.000	14.697	1.017±0.009	1.268±0.022	0.913±0.013	0.787±0.012
vii	0.225	0.200	6.000	8.573	1.002±0.044	1.221±0.050	1.048±0.002	0.891±0.024
viii	0.225	0.300	6.000	6.532	1.002±0.018	0.989±0.086	1.000±0.002	1.007±0.055
ix	0.225	0.400	6.000	5.511	1.001±0.013	1.034±0.018	1.026±0.002	0.994±0.010
x	0.225	0.500	6.000	4.899	1.003±0.004	1.000±0.003	1.000±0.002	1.000±0.002
xi	0.225	0.300	1.000	2.667	0.994±0.021	0.956±0.124	1.000±0.011	1.028±0.085
xii	0.225	0.300	3.000	4.619	0.993±0.046	0.982±0.019	1.000±0.003	1.011±0.013
xiii	0.225	0.300	6.000	6.532	1.002±0.018	0.989±0.086	1.000±0.002	1.007±0.055
xiv	0.225	0.300	10.000	8.433	0.992±0.007	0.995±0.127	1.000±0.002	1.003±0.080
xv	0.225	0.300	20.000	11.926	0.993±0.005	1.027±0.040	1.000±0.003	0.984±0.024

References

(1) Verway, E. J. W.; Overbeek, J. T. G. *Theory of The Stability of Lyophobic Colloids*; Elsevier Publ. Co. Inc.: New York, 1948.

(2) Lindner, P.; Zemb, T. *Neutron, X-rays and Light. Scattering Methods Applied to Soft Condensed Matter*; North-Holland: Amsterdam, 2002.

(3) Henderson, R. L. A uniqueness theorem for fluid pair correlation functions. *Phys. Lett.* **1974**, *49A*, 197–198.

(4) Gray, C. G.; Gubbins, K. E. *Theory of Molecular Fluids: Fundamentals Volume I*; Clarendon Press: Oxford, 1984.

(5) Egelstaff, P. A. *An Introduction to the Liquid State, 2nd Ed.*; Clarendon Press: Oxford, 1992.

(6) Hansen, J.-P.; McDonald, I. R. *Theory of Simple Liquids with Applications to Soft Matter, 4th Ed.*; Academic Press: Amsterdam, 2013.

(7) Lee, L. L. The potential distribution-based closures to the integral equations for liquid structure: The Lennard-Jones fluid. *J. Chem. Phys.* **1997**, *107*, 7360–7370.

(8) Hayter, J. B.; Penfold, J. An analytic structure factor for macroion solutions. *Mol. Phys.* **1981**, *42*, 109–118.

(9) Hansen, J.-P.; Hayter, J. B. A rescaled MSA structure factor for dilute charged colloidal dispersions. *Mol. Phys.* **1982**, *46*, 651–656.

(10) Snook, I. K.; Hayter, J. B. Static Structure of Strongly Interacting Colloidal Particles. *Langmuir* **1992**, *8*, 2880–2884.

(11) Beresford-Smith, B.; Chan, D. Y. C.; Mitchell, D. J. The electrostatic interaction in colloidal systems with low added electrolyte. *J. Colloid Interface Sci.* **1985**, *105*, 216–234.

(12) Belloni, L. *Neutron, X-Ray and Light Scattering: Introduction to an Investigative Tool for Colloidal and Polymetric Systems*; edited by Th. Zemb and P. Lindner, North-Holland, Amsterdam, 1991; pp 135–155.

(13) Klein, R.; D'Aguanno, B. *Light Scattering: Principles and Development*; edited by W. Brown, Clarendon Press, Oxford, 1996; pp 30–102.

(14) Heinen, M.; Holmqvist, P.; Banchio, A. J.; Nägele, G. Pair structure of the hard-sphere Yukawa fluid: An improved analytic method versus simulations, Rogers-Young scheme, and experiment. *J. Chem. Phys.* **2011**, *134*, 044532.

(15) Gillan, M. A simple model for the classical one-component plasma. *Journal of Physics C: Solid State Physics* **1974**, *7*, L1.

(16) Schmitz, K. S. *Macroions in Solution and Colloidal Suspension*; Wiley-VCH, New York, 1992.

(17) Rogers, F. J.; Young, D. A. New, thermodynamically consistent, integral equation for simple fluids. *Phys. Rev. A* **1984**, *30*, 999–1007.

(18) Huš, M.; Zalar, M.; Urbic, T. Correctness of certain integral equation theories for core-softened fluids. *J. Chem. Phys.* **2013**, *138*, 224508.

(19) Anta, J. A.; Lago, S. Self-consistent effective interactions in charged colloidal suspensions. *J. Chem. Phys.* **2002**, *116*, 10514–10522.

(20) Rasmussen, C. E.; Williams, C. K. I. *Gaussian Processes for Machine Learning*; The MIT Press, Cambridge, 2006; pp 1–31.

(21) Chang, M.-C.; Tung, C.-H.; Chang, S.-Y.; Carrillo, J.-M.; Wang, Y.; Sumpter, B. G.; Huang, G.-R.; Do, C.; Chen, W.-R. A machine learning inversion scheme for determining interaction from scattering. *Commun. Phys.* **2022**, *5*, 46.

(22) Tung, C.-H.; ; Chang, S.-Y.; Chang, M.-C.; Carrillo, J.-M.; Sumpter, B. G.; Do, C.; Chen, W.-R. Inferring colloidal interaction from scattering by machine learning. *Carbon Trends* **2023**, *10*, 100252.

(23) Hynninen, A.-P.; Dijkstra, D. Phase diagrams of hard-core repulsive Yukawa particles. *Phys. Rev. E* **2003**, *68*, 021407.

(24) Kingma, D. P.; Ba, J. Adam: A method for stochastic optimization. *arXiv preprint arXiv:1412.6980* **2014**,

(25) Byrd, R. H.; Lu, P.; Nocedal, J.; Zhu, C. A limited memory algorithm for bound constrained optimization. *SIAM J. Sci. Comput.* **1995**, *16*, 1190–1208.

(26) Virtanen, P. et al. SciPy 1.0: Fundamental algorithms for scientific computing in Python. *Nat. Methods* **2020**, *17*, 261–272.

(27) Russ, C.; von Grünberg, H. H.; Dijkstra, D.; van Roij, R. Three-body forces between charged colloidal particles. *Phys. Rev. E* **2002**, *66*, 011402.

(28) Hynninen, A.-P.; Dijkstra, D.; ; van Roij, R. Effect of three-body interactions on the phase behavior of charge-stabilized colloidal suspensions. *Phys. Rev. E* **2004**, *69*, 061407.

TOC Graphic